Applied Physics Letters

Dynamics of NEMS resonators across dissipation limits

Cite as: Appl. Phys. Lett. **121**, 023506 (2022); https://doi.org/10.1063/5.0100318
Submitted: 23 May 2022 • Accepted: 28 June 2022 • Published Online: 12 July 2022

C. Ti, J. G. McDaniel, A. Liem, et al.

Dynamics of NEMS resonators across dissipation limits

Cite as: Appl. Phys. Lett. **121**, 023506 (2022); doi: 10.1063/5.0100318
Submitted: 23 May 2022 · Accepted: 28 June 2022 ·
Published Online: 12 July 2022

C. Ti,[1] J. G. McDaniel,[1] A. Liem,[1] H. Gress,[1] M. Ma,[1] S. Kyoung,[1] O. Svitelskiy,[2] C. Yanik,[3] I. I. Kaya,[3,4] M. S. Hanay,[5,6] M. González,[7] and K. L. Ekinci[1,a)]

AFFILIATIONS

[1]Department of Mechanical Engineering, Division of Materials Science and Engineering, and the Photonics Center, Boston University, Boston, Massachusetts 02215, USA
[2]Department of Physics, Gordon College, Wenham, Massachusetts 01984, USA
[3]SUNUM, Nanotechnology Research and Application Center, Sabanci University, Istanbul 34956, Turkey
[4]Faculty of Engineering and Natural Sciences, Sabanci University, Istanbul 34956, Turkey
[5]Department of Mechanical Engineering, Bilkent University, Ankara 06800, Turkey
[6]UNAM – Institute of Materials Science and Nanotechnology, Bilkent University, Ankara 06800, Turkey
[7]Aramco Services Company, Aramco Research Center—Houston, Houston, Texas 77084, USA

[a)]Author to whom correspondence should be addressed: ekinci@bu.edu

ABSTRACT

The oscillatory dynamics of nanoelectromechanical systems (NEMS) is at the heart of many emerging applications in nanotechnology. For common NEMS, such as beams and strings, the oscillatory dynamics is formulated using a dissipationless wave equation derived from elasticity. Under a harmonic ansatz, the wave equation gives an undamped free vibration equation; solving this equation with the proper boundary conditions provides the undamped eigenfunctions with the familiar standing wave patterns. Any harmonically driven solution is expressible in terms of these undamped eigenfunctions. Here, we show that this formalism becomes inconvenient as dissipation increases. To this end, we experimentally map out the position- and frequency-dependent oscillatory motion of a NEMS string resonator driven linearly by a non-symmetric force at one end at different dissipation limits. At low dissipation (high Q factor), we observe sharp resonances with standing wave patterns that closely match the eigenfunctions of an undamped string. With a slight increase in dissipation, the standing wave patterns become lost, and waves begin to propagate along the nanostructure. At large dissipation (low Q factor), these propagating waves become strongly attenuated and display little, if any, resemblance to the undamped string eigenfunctions. A more efficient and intuitive description of the oscillatory dynamics of a NEMS resonator can be obtained by superposition of waves propagating along the nanostructure.

Nanoelectromechanical systems (NEMS) have enabled a number of nanotechnologies for monitoring the environment,[1] storing and processing information,[2,3] and applying controllable forces to physical[4] and biological nanosystems.[5,6] NEMS-based detection of individual atoms and molecules,[7,8] single charge quanta,[9,10] and vibrations of single microorganisms[11,12] has established the potential of NEMS sensors. NEMS are also at the forefront of fundamental physical science, opening up studies in quantum mechanics,[13] optomechanics,[14] Brownian motion,[15,16] fluid mechanics,[17–20] and nanoelectronics.[21–24]

In a typical implementation,[25] one actuates linear oscillations of the NEMS resonator using a force transducer and looks for changes in the phase, frequency, or dissipation due to interactions. For proper operation, the user must know how exactly the nanomechanical structure is moving under the actuation forces. The oscillatory NEMS dynamics is typically determined using a dissipationless wave equation, e.g., the beam equation or the string equation, derived from elasticity. After the harmonic ansatz, one obtains the undamped free vibration equation and solves it subject to boundary conditions.[26,27] This approach provides the undamped eigenfunctions that correspond to standing wave patterns on the structure. These well-known patterns emerge from the interference of undamped waves reflecting back and forth from the boundaries of the structure. The undamped eigenfunctions form a complete set, and the driven harmonic motion of NEMS, even in the presence of dissipation, can be expressed as an expansion in terms of these eigenfunctions.[26–30] The practical aspects of the expansion, however, become cumbersome with increasing dissipation.

Since waves get attenuated along the structure and at the boundaries, one needs a large, if not infinite, number of terms in the eigenfunction expansion. Here, we illustrate these complications by examining the position- and frequency-dependent oscillatory dynamics of a NEMS resonator driven by a non-symmetric harmonic force at different dissipation limits. Instead of an expansion including a large number of undamped eigenfunctions, we describe the dynamics efficiently by superposing waves that are attenuated along the beam.

Our experiments are performed on silicon nitride doubly clamped beams with respective linear dimensions along x, y, and z axes of $l \times b \times h \approx 50\,\mu\text{m} \times 900\,\text{nm} \times 100\,\text{nm}$, all from the same batch. There is a 2-μm gap between the beam and the substrate. The beams are under tension as inferred from their resonance frequencies in vacuum[21] and behave as strings. Figure 1(a) shows a scanning electron microscope (SEM) image of a beam. The two identical u-shaped gold electrodes are electrothermal actuators for driving the out-of-plane (z-axis) flexural motion of the beam [Fig. 1(a), inset]. Each actuator is patterned on one anchor of the resonator with a thickness of 135 nm and a width of 120 nm. The actuator spans the undercut region and the beam, with $\xi_1 = 800$ nm and $\xi_2 = 600$ nm; its electrical resistance is $3.54 \pm 0.1\,\Omega$.[21] We apply a sinusoidal current at frequency f to only one actuator, e.g., the actuator on the left in Fig. 1(a). Joule heating generates temperature oscillations in the actuator at $2f$. Owing to the mismatch between the thermal expansion coefficients of the gold and silicon nitride layers, a bending moment develops and drives out-of-plane flexural oscillations of the beam at $2f$. Figure 1(b) shows results from our finite element models of the electrothermal actuator in vacuum. The black curve in Fig. 1(b) is the input current waveform at $f = 2.5895$ MHz, with instantaneous temperature fields [Fig. 1(b), top] over the suspended base region of a 50-μm resonator. The red curve in Fig. 1(b) displays the simulated amplitude of the resonator at its center at $2f = 5.179$ MHz. For 1 mA rms input current at $f = 2.5895$ MHz, the temperature oscillates with rms values of $\Delta T_v = 0.1$ K and $\Delta T_w = 0.05$ K in vacuum and water (not shown), respectively. The power dissipated on the actuator remains constant over our frequency range.[15,21] For fixed power, the attenuation of ΔT_v as a function of frequency is negligible;[31] the attenuation of ΔT_w is expected be even less due to the added thermal conductance of water. Hence, the actuation force is assumed to be independent of frequency.

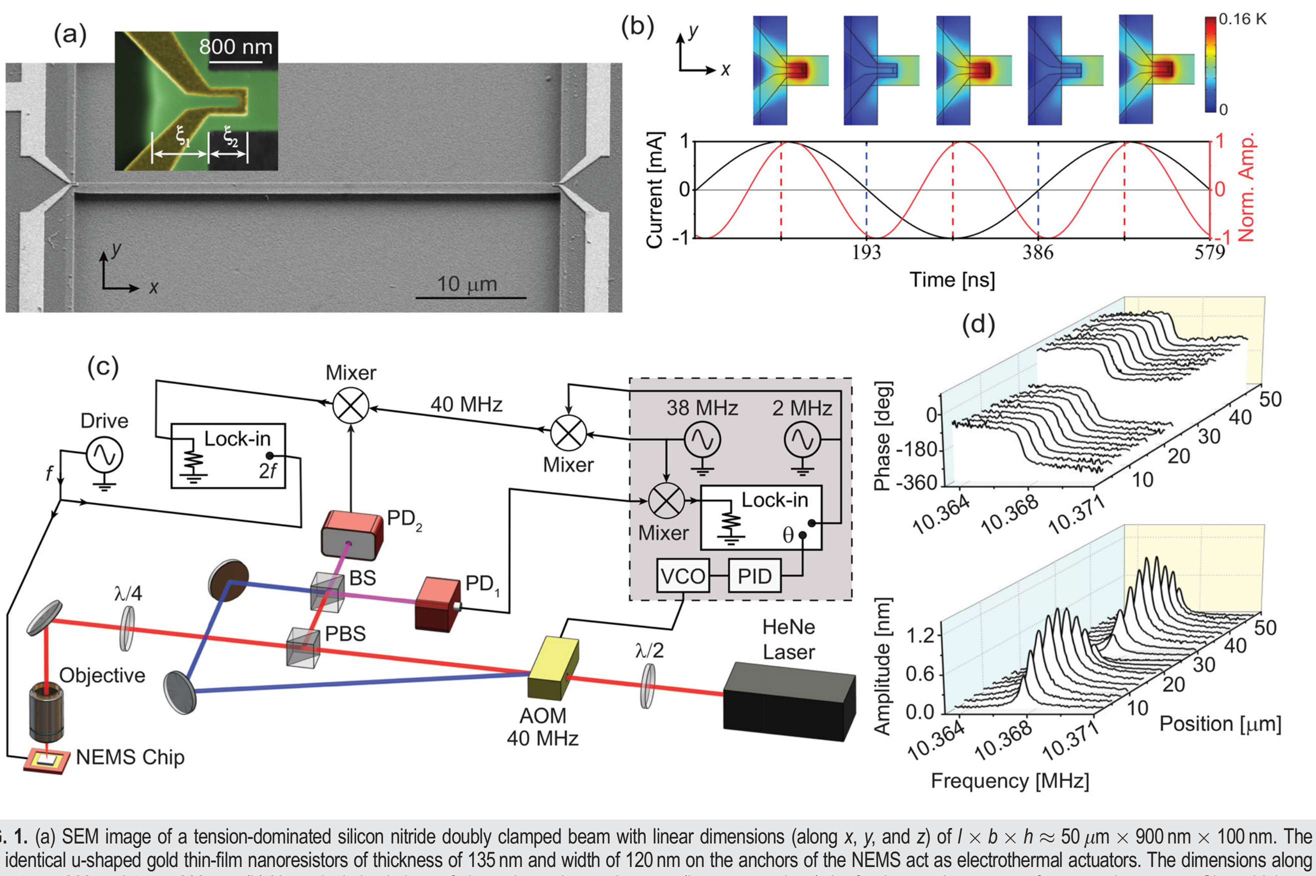

FIG. 1. (a) SEM image of a tension-dominated silicon nitride doubly clamped beam with linear dimensions (along x, y, and z) of $l \times b \times h \approx 50\,\mu\text{m} \times 900\,\text{nm} \times 100\,\text{nm}$. The two identical u-shaped gold thin-film nanoresistors of thickness of 135 nm and width of 120 nm on the anchors of the NEMS act as electrothermal actuators. The dimensions along x are $\xi_1 \approx 800$ and $\xi_2 \approx 600$ nm. (b) Numerical simulations of electrothermal actuation near (but not exactly at) the fundamental resonance frequency in vacuum. Sinusoidal current input to the nanoresistor at $f = 2.5895$ MHz (black curve) results in nanomechanical oscillations of the beam at $f = 5.179$ MHz. The response of the beam at its center is shown. The small phase between the current and displacement is due to the thermal inertia and the mechanical response of the resonator. The color maps are the temperature profiles of the region in the inset of (a) at five instants. Typical powers dissipated on the nanoresistor are 1, 50, and 100 μW in vacuum, air, and water, respectively. (c) Heterodyne optical interferometer. AOM: acousto-optic modulator; $\lambda/2$: half wave plate; $\lambda/4$: quarter wave plate; PBS: polarizing beam splitter; BS: beam splitter; PD: photodetector; PID: proportional-integral-derivative controller; VCO: voltage controlled oscillator. The signal on PD_1 is used for feedback; PD_2 is connected to a lock-in amplifier via a mixer for driven measurements. The lock-in amplifier is used in the $2f$ mode. (d) Phase (top) and amplitude for a beam as functions of frequency and position at its first harmonic resonance in vacuum.

The harmonically driven linear dynamics of the NEMS resonator, i.e., the rms amplitude W_{rms} and phase ϕ of its oscillations as functions of position, is measured in a heterodyne optical interferometer.[21] Figure 1(c) shows the schematic diagram of the optical setup.[21,32] An XYZ stage is used to position the laser spot along the x axis in Fig. 1(a). Figure 1(d) shows a representative dataset: W_{rms} and ϕ as a function of x and drive frequency for the first harmonic mode resonance of the NEMS in vacuum. The measured ϕ can be understood as the phase of the NEMS oscillation with respect to the sinusoidal drive force and includes all the parasitic phases coming from the measurement circuit. We perform the measurements in vacuum, air, and water, correspondingly, respectively, to the low ($Q \gtrsim 10^4$), intermediate ($20 \lesssim Q \lesssim 70$), and high dissipation ($Q \sim 1$) regimes. In vacuum and air, we measure the resonator amplitude and phase around the resonance frequencies (supplementary material, Figs. S1 and S2); in water, we sweep the frequency over our entire frequency range.

We first discuss the oscillatory dynamics of the NEMS at very low dissipation ($Q \approx 20 \times 10^3$), as shown in Fig. 2. From measurements shown in supplementary material, Fig. S1, we obtain the spatial dependence of the rms resonance amplitude W_{rms} and the relative phase ϕ_{rel} at each resonance frequency $f_n = \frac{\omega_n}{2\pi}$ [Figs. 2(a)–2(c)]. W_{rms} are the peak values in the amplitude vs frequency curve for each resonance (Fig. S1), and ϕ_{rel} is the phase with respect to the phase of the first data point around $x = 0$, i.e., $\phi_{rel}(x) = \phi(x) - \phi\,(x = 2.5\,\mu\text{m})$, at f_n. The time-dependent motion of the beam at frequency f_n can be reconstructed from W_{rms} and ϕ_{rel} as $w(x,t) = \sqrt{2}W_{rms}(x)\sin[\omega_n t + \phi_{rel}(x)]$ by advancing the dimensionless time $\omega_n t$ over a cycle. Figures 2(d)–2(f) shows normalized $w(x, t)$ for the first three modes. The supplementary material includes video files of these modes.

Since Q is very high, we ignore the dissipation and solve the undamped string equation with fixed–fixed boundary conditions to obtain $w(x,t) = \sin(k_n x)\sin(\omega_n t)$ with n being the mode number.[33] Here, $k_n = n\frac{\pi}{l}$ is the wave number, and $f_n = \frac{\omega_n}{2\pi} = n\frac{c}{2l}$ is the corresponding eigen-frequency. The speed of flexural waves in the beam is $c = \sqrt{\frac{\tau}{\mu}} = 510 \pm 10\,\text{m/s}$, based on experimental values[21] of tension $\tau = 68 \pm 4\,\mu\text{N}$ and mass per unit length $\mu = \rho_s bh = 26.6 \pm 0.3 \times 10^{-11}\,\text{kg/m}$ with the density being $\rho_s = 2960 \pm 30\,\text{kg/m}^3$. The shadings in Figs. 2(a)–2(c) are based on this solution for $n = 1$, 2, and 3. We note that $w(x, t)$ can also be written as a sum of two undamped propagating waves as $w(x,t) = \Re\left\{\frac{1}{2}e^{i(k_n x - \omega_n t)} - \frac{1}{2}e^{-i(k_n x + \omega_n t)}\right\}$, with $\Re$ denoting the real part of the complex expression. We emphasize that the boundary conditions are not trivial: there are undercuts and

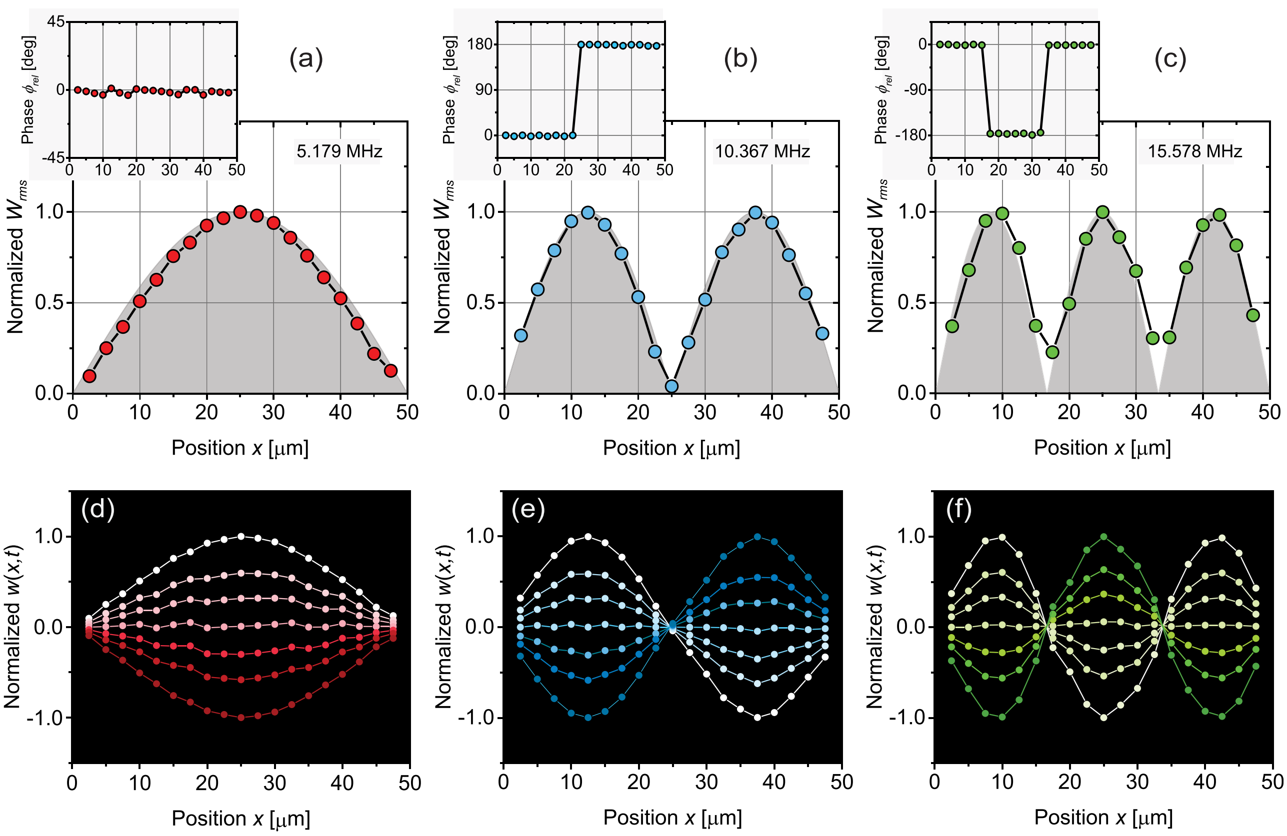

FIG. 2. Oscillatory dynamics of a 50-μm-long resonator at the low dissipation limit, i.e., in vacuum. (a)–(c) Normalized rms amplitudes W_{rms} and relative phases ϕ_{rel} (insets) of the beam oscillations, as a function of x for its first three modes. Data points are from measurements, and the background shadings are $|\sin(\frac{n\pi}{l}x)|$. The phase values change by exactly 180° at the nodes. (d)–(f) Normalized time-dependent amplitude $w(x, t)$ for the first three modes, as a function of x during an oscillation cycle. Relevant parameters of the modes are listed in Table I.

TABLE I. Parameters for the first three modes of the NEMS resonator in vacuum and air: $\omega_n/2\pi$ and Q_n, respectively, refer to the mode frequency and quality factor; k_n is the mode wave number. Air values are indicated by *a*; *R* and *I* correspond to real and imaginary components, respectively.

	Vacuum			Air			
Mode	$\frac{\omega_n}{2\pi}$ (MHz)	Q_n	k_n (m^{-1})	$\frac{\omega_n^{(a)}}{2\pi}$ (MHz)	$Q_n^{(a)}$	$k_{nR}^{(a)}$ (m^{-1})	$k_{nI}^{(a)}$ (m^{-1})
1	5.179	23.6×10^3	6.28×10^4	5.163	32 ± 5	6.58×10^4	2.21×10^3
2	10.367	22.8×10^3	12.57×10^4	10.315	54 ± 5	13.18×10^4	3.76×10^3
3	15.578	20.3×10^3	18.85×10^4	15.504	73 ± 5	19.76×10^4	4.04×10^3

the gold nanoresistors around $x = 0$ and $x = l$. The rigidity of the beam also becomes appreciable near the clamps. Regardless, the low dissipation makes these complications negligible.

Now, we turn to the oscillatory dynamics of the same resonator in the intermediate dissipation limit by repeating the experiment in air. Since the quality factors, $Q_n^{(a)}$, in air are still relatively high (Table I), the modes are well separated in frequency (supplementary material, Fig. S2). At a first glance, W_{rms} and ϕ_{rel} data in Figs. 3(a)–3(c) look similar to those in Fig. 2. The resonance frequencies also do not deviate much from their vacuum values (Table I). Upon more careful comparison with Fig. 2, however, we notice that the amplitudes in Fig. 3 become asymmetric with respect to the beam center and decay noticeably away from the actuator. To highlight these features, we show in the background of Figs. 3(a)–3(c) the undamped eigenfunctions $|\sin(\frac{n\pi}{l}x)|$. The step jumps in ϕ_{rel} in Figs. 2(b) and 2(c) become smooth in Figs. 3(b) and 3(c), indicating that the waves are propagating along the x. The corresponding $w(x, t)$ constructed from the data is shown in Figs. 3(d)–3(f). Supporting Information includes video files, where the zero crossings of $w(x, t)$ move slightly along the x.

We model the dynamics in air using the string equation with uniform viscous damping,[15,21,33–35]

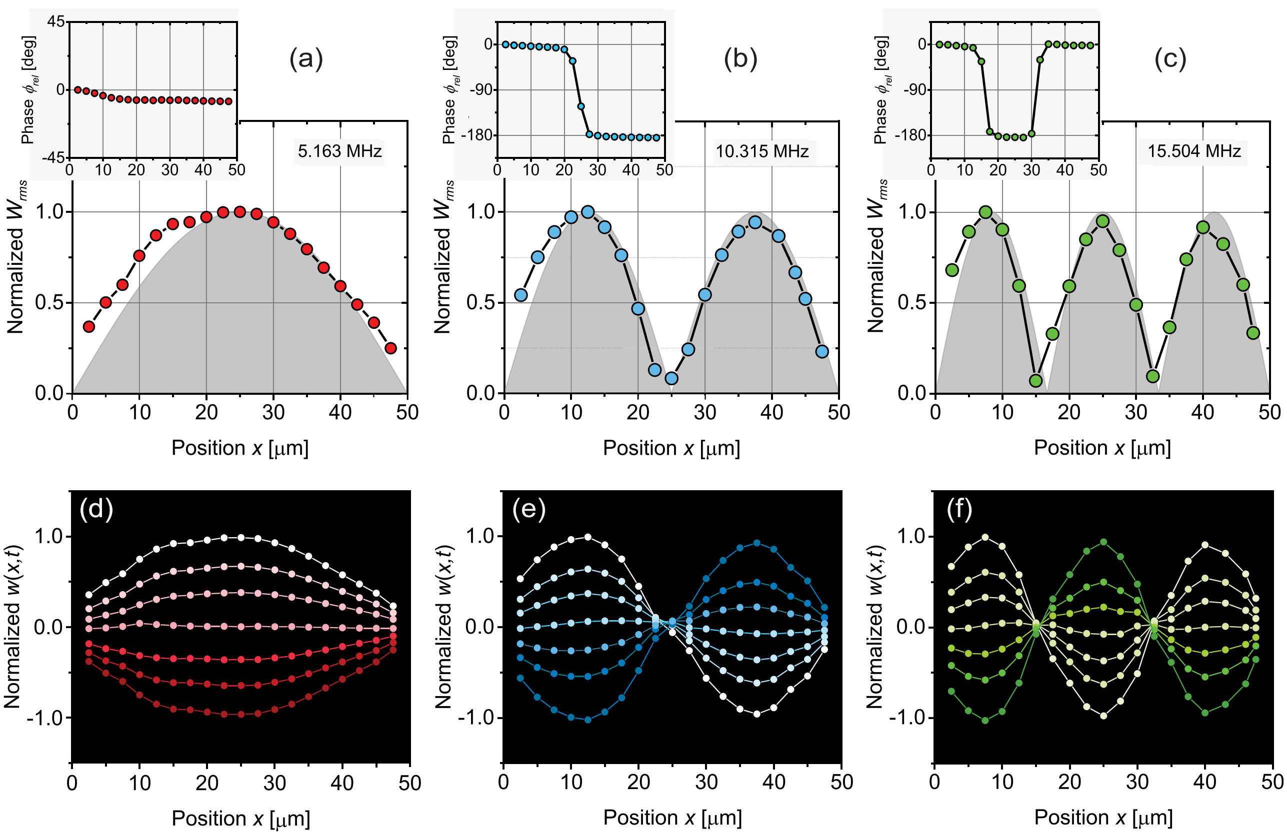

FIG. 3. Oscillatory dynamics of the 50-μm resonator at intermediate dissipation. (a)–(c) Normalized rms amplitude W_{rms} and relative phase ϕ_{rel} (insets) of the beam, as a function of x for its first three modes. Data points are from measurements, and the background shadings are $|\sin(\frac{n\pi}{l}x)|$. (d)–(f) Normalized $w(x, t)$ for the first three resonances, as a function of x during the oscillation cycle. Relevant parameters of the modes are listed in Table I.

$$\mu \frac{\partial^2 w}{\partial t^2} + \gamma \frac{\partial w}{\partial t} - \tau \frac{\partial^2 w}{\partial x^2} = f(x,t). \quad (1)$$

Here, γ is the damping per unit length and $f(x,t) = \Re\{F(x)e^{i\omega t}\}$ is the applied force per unit length with $F(x)$ being the complex force amplitude. Considering only the domain $\xi_1 + \xi_2 < x \leq l$ in which $F(x) \approx 0$, we write the general solution to Eq. (1) as

$$w(x,t) = \Re\{Ae^{i(kx-\omega t)} + Be^{-i(kx+\omega t)}\}. \quad (2)$$

The complex wave vector k is found as

$$k = k_R + ik_I = \frac{\omega}{c}\left(1 + i\frac{\gamma}{\mu\omega}\right)^{1/2}, \quad (3)$$

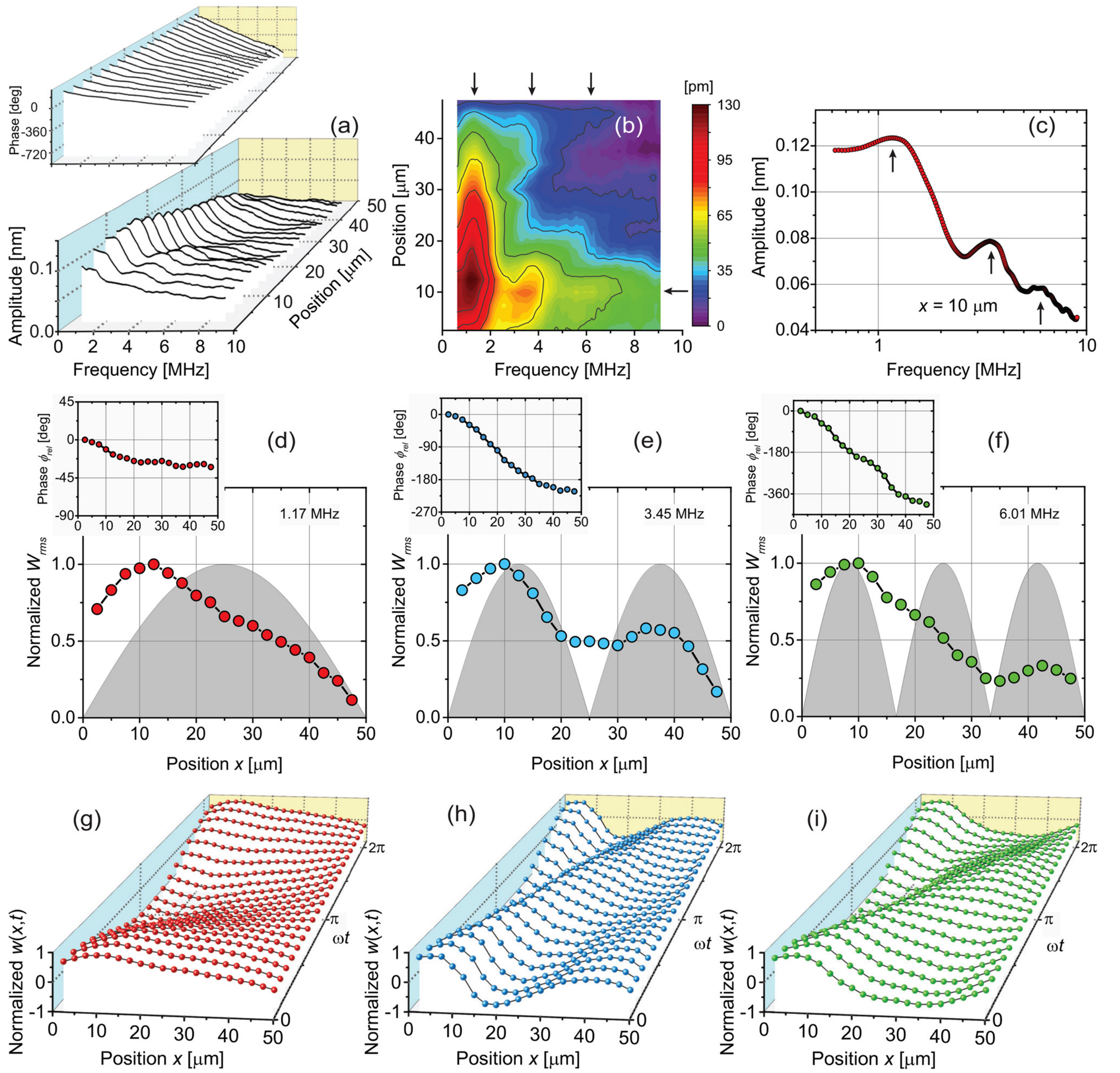

FIG. 4. Oscillatory dynamics of the 50-μm resonator at high dissipation. (a) W_{rms} and phase (inset) of the resonator as a function of drive frequency at different x positions on the resonator. (b) Color map of W_{rms}. (c) W_{rms} as a function of frequency at $x = 10\,\mu$m, with peaks corresponding to the first three resonances. (d)–(f) Normalized W_{rms} as a function of x at the peak frequencies in (c) [vertical arrows in (b)]: 1.17, 3.45, and 6.01 MHz. The insets show ϕ_{rel}. (g)–(i) Normalized $w(x, t)$ constructed from the data in (d)–(f). A wave propagates from $x \approx 0$ to $x \approx l$ in all cases. The wave decays at different length scales.

where $k_R = \Re\{k\}$, $k_I = \Im\{k\}$, and $\Re$ and $\Im$, respectively, denote the real and imaginary components. Equation (2) can, thus, be rewritten as

$$w(x,t) = \Re\{Ae^{-k_I x}e^{i(k_R x - \omega t)} + Be^{k_I x}e^{-i(k_R x + \omega t)}\} \tag{4}$$

with A and B being the complex amplitudes of the right- and left-propagating waves, respectively. We can fit the data in Figs. 3(a)–3(c) using Eq. (4), as shown in Fig. S3. The best fits provide the complex k values listed in Table I. Using $\gamma \approx \frac{\mu\omega}{Q_n^{(a)}}$, we expand Eq. (3) to find $k_n^{(a)} \approx \frac{n\pi}{l}(1 + i\frac{1}{2Q_n^{(a)}})$. The values for $k_{nR}^{(a)}$ are very close to $\frac{n\pi}{l}$; $k_{nI}^{(a)}$ is roughly a factor of two to three larger than $\frac{n\pi}{2lQ_n^{(a)}}$. We note that the fits in Fig. S3 are approximations only and can be improved by modeling the boundary conditions more realistically.

Finally, we show our results on the oscillatory dynamics of the resonator at the high dissipation limit ($Q \approx 1$) in Fig. 4. This experiment is performed with the NEMS immersed in water. Figure 4(a) shows the rms oscillation amplitude and the phase (inset) of the NEMS as a function of frequency and position, obtained by scanning the drive frequency in the $0.6 - 9$ MHz range at each x. The colormap in Fig. 4(b) is the top view of the amplitude from Fig. 4(a), showing how the amplitude decays with frequency and position. We observe that the amplitude shows peaks at some frequencies reminiscent of resonances. For instance, W_{rms} as a function of frequency at $x = 10\,\mu$m shown in Fig. 4(c) has three peaks. Taking the values of W_{rms} and phase at frequencies marked by the vertical arrows in Fig. 4(b), i.e., at 1.17, 3.45, and 6.01 MHz, we obtain the position dependent data for W_{rms} and ϕ_{rel} shown in Figs. 4(d)–4(f) at the peak frequencies in Fig. 4(c). For more insight into the motion of the beam, we construct $w(x, t)$ as above for full cycles of oscillation, as shown in Figs. 4(g)–4(i) and supplementary material, videos. Immediately evident is the fact that $w(x, t)$ are traveling waves that are generated at the actuator at $x \approx 0$ and move toward $x = l$. The waves decay significantly over the length of the beam. Consequently, we can neglect the wave propagating to the left in Eq. (2) and have a simpler mathematical description,

$$\begin{aligned} w(x,t) &\approx \Re\{Ae^{i(kx-\omega t)}\} \\ &= A'e^{-k_I x}\cos(k_R x - \omega t + \varphi), \end{aligned} \tag{5}$$

where the phase φ is adjusted such that A' is real. To estimate k_R and k_I as a function of frequency, we advance the waveform in time (or adjust φ) until we obtain a peak near the $x = 0$ anchor. This results in datasets such as those shown in Fig. 5(a). In these semilogarithmic graphs, $|w(x,t)|$ is plotted at four frequencies with the x' axis starting at the peak position. The distance between successive peaks is half the wavelength and provides an estimate for k_R of a given dataset. The decaying exponential envelope of each dataset, shown by the line in each plot, provides an estimate for k_I. In Fig. 5(b), the extracted k_R and k_I are plotted as functions of frequency (lower x-axis) and the viscous boundary layer thickness (upper x-axis) generated by the oscillations, $\delta = \sqrt{\frac{2\eta_f}{\rho_f\omega}}$, where ρ_f and η_f are the density and dynamic viscosity of the water, respectively. The k_R data start from 3 MHz since it is impractical to measure the wavelength in the absence of two or more peaks.

We now show how the frequency-dependent spatial profile of driven NEMS oscillations can be related to the physical properties of the fluid by using Stokes' theory of the oscillating cylinder in a viscous fluid.[20,29,30] We Fourier transform the undamped string equation

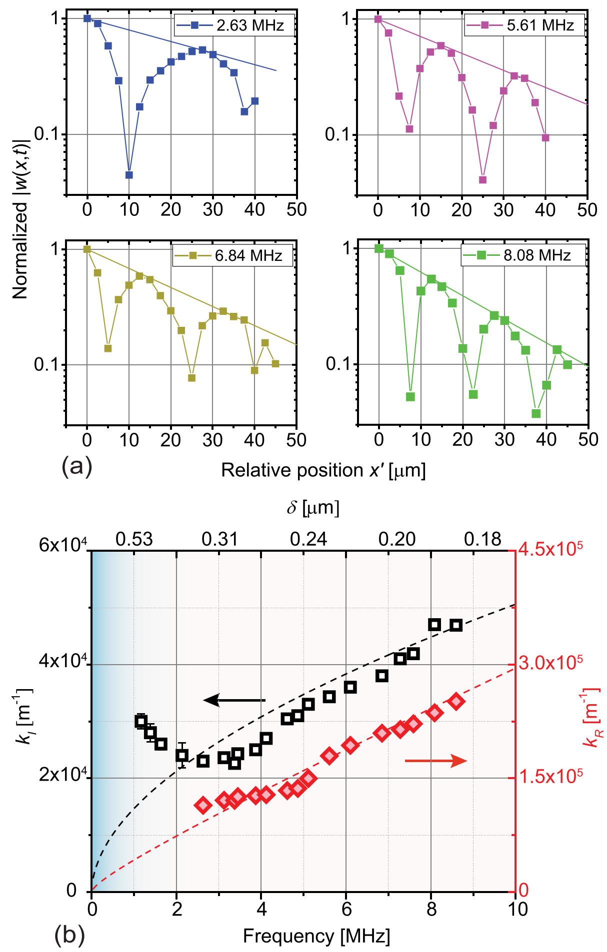

FIG. 5. (a) Semilogarithmic plots showing normalized $|w(x,t)|$ vs x' at different drive frequencies, where $x' = 0$ marks the peak position of the waveform. Fitting the envelope with a decaying exponential (lines) provides k_I; the distance between successive peaks provides k_R. (b) k_I (left y) and k_R (right y) as a function of frequency. The upper x axis shows δ. The shading indicates the regions $\delta \gtrsim$ gap (dark) and $\delta \lesssim$ gap (light). The dashed curves show theoretical predictions. Error bars are the uncertainties in the linear fits in (a).

[$\gamma = 0$ and $f(x,t) = 0$ in Eq. (1)] in both space and time with the fluid providing the only force (per unit length), $\tilde{F}_f(k,\omega)$, on the beam,

$$(-\omega^2\mu + \tau k^2)\tilde{W}(k,\omega) = \tilde{F}_f(k,\omega). \tag{6}$$

The fluid force is[29]

$$\begin{aligned} \tilde{F}_f(k,\omega) &\approx \frac{\pi}{4}\rho_f\omega^2 b^2\Gamma_b(\omega)\tilde{W}(k,\omega) \\ &\approx \mu\omega^2 T_0\Gamma_b(\omega)\tilde{W}(k,\omega), \end{aligned} \tag{7}$$

where $\Gamma_b(\omega) = \Gamma_b'(\omega) + i\Gamma_b''(\omega)$ is the hydrodynamic function of a blade (found from the cylinder solution[30]), $\mu = \rho_s bh$ is the mass per unit length of the string, and ρ_f and η_f are, respectively, subsumed into $T_0 = \frac{\pi}{4}\frac{\rho_f b}{\rho_s h}$ and $\Gamma_b(\omega)$. Substituting $\tilde{F}_f(k,\omega)$ into Eq. (6), we obtain

$$k_R + ik_I = \frac{\omega}{c}\sqrt{\left(1 + T_0\Gamma_b'(\omega)\right) + iT_0\Gamma_b''(\omega)} \quad (8)$$

indicating that one can determine ρ_f and η_f from measured k_R and k_I. This approach could be complementary to that based on fitting the frequency response of the NEMS at a single point. In fact, this theory can be extended to obtain properties of viscoelastic fluids as well.[36,37]

The dashed line in Fig. 5(b) shows k_R and k_I predicted from Eq. (8) using experimental values of c and T_0 and calculated $\Gamma_b(\omega)$. These predictions match well with our experimental data for frequencies $\gtrsim 2.5$ MHz. The measured k_I deviates from theory at low frequency because of the added squeeze damping.[20]

As more emphasis is put on precision measurements in fluids,[38,39] the spatial decay of the amplitude of driven NEMS resonators could have significant implications. For NEMS-based mass sensing and mass spectrometry, deconvoluting the mass and position of the adsorbed analyte molecule on the NEMS from frequency shifts requires a detailed knowledge of the oscillatory amplitude of the resonator in multiple modes.[8,40] Of particular importance is the behavior of the nodes in the intermediate dissipation regime: since there is a traveling wave along the structure with a small amplitude, there are no true nodes. Similarly, in dynamic AFM experiments in air and liquids,[6] the position of the drive force along the microcantilever should affect the tip amplitude and tip-sample interactions. Another relevant area is fundamental studies in fluid dynamics using NEMS and microcantilever resonators.[15,29] The accuracy of an eigenfunction expansion containing a few eigenmodes should be assessed carefully in liquids.[15,29] In summary, our results here will be of relevance to research and technology involving NEMS, AFM, and even macroscopic mechanical resonators.

See the supplementary material for three figures and nine videos. The supplementary figures show the resonator amplitude and phase around the resonances in vacuum and air and wave fits to air data. The supplementary videos show the time-dependent motion of the beam at different dissipation limits.

We acknowledge support from the U.S. NSF (Nos. CBET 1604075, CMMI 1934271, CMMI 2001403, DMR 1709282, CMMI 1661700, and CMMI 1934370). We thank Atakan B. Ari for help with sample fabrication.

AUTHOR DECLARATIONS

Conflict of Interest

The authors have no conflicts to disclose.

Author Contributions

Chaoyang Ti: Conceptualization (equal); Data curation (lead); Formal analysis (lead); Investigation (lead); Methodology (equal); Validation (lead); Writing – original draft (lead); Writing – review and editing (equal). **M. Selim Hanay:** Resources (equal). **Miguel Gonzàlez:** Resources (equal). **Kamil L. Ekinci:** Conceptualization (equal); Funding acquisition (lead); Methodology (equal); Supervision (lead); Writing – original draft (equal); Writing – review and editing (lead). **James G. McDaniel:** Conceptualization (equal); Methodology (lead). **Alyssa Tomoko Liem:** Methodology (equal). **Hagen Gress:** Investigation (supporting). **Monan Ma:** Software (equal). **Sumin Kyoung:** Software (supporting). **Oleksiy Svitelskiy:** Investigation (supporting). **Cenk Yanik:** Resources (equal). **Ismet Inonu Kaya:** Resources (equal).

DATA AVAILABILITY

The data that support the findings of this study are available from the corresponding author upon reasonable request.

REFERENCES

1. I. Bargatin, E. Myers, J. Aldridge, C. Marcoux, P. Brianceau, L. Duraffourg, E. Colinet, S. Hentz, P. Andreucci, and M. Roukes, "Large-scale integration of nanoelectromechanical systems for gas sensing applications," Nano Lett. **12**, 1269–1274 (2012).
2. L. Fan, C.-L. Zou, M. Poot, R. Cheng, X. Guo, X. Han, and H. X. Tang, "Integrated optomechanical single-photon frequency shifter," Nat. Photonics **10**, 766–770 (2016).
3. P. Rabl, S. J. Kolkowitz, F. Koppens, J. Harris, P. Zoller, and M. D. Lukin, "A quantum spin transducer based on nanoelectromechanical resonator arrays," Nat. Phys. **6**, 602–608 (2010).
4. Y.-I. Sohn, S. Meesala, B. Pingault, H. A. Atikian, J. Holzgrafe, M. Gündoğan, C. Stavrakas, M. J. Stanley, A. Sipahigil, J. Choi *et al.*, "Controlling the coherence of a diamond spin qubit through its strain environment," Nat. Commun. **9**, 2012 (2018).
5. B. T. Marshall, M. Long, J. W. Piper, T. Yago, R. P. McEver, and C. Zhu, "Direct observation of catch bonds involving cell-adhesion molecules," Nature **423**, 190–193 (2003).
6. A. Raman, S. Trigueros, A. Cartagena, A. Stevenson, M. Susilo, E. Nauman, and S. A. Contera, "Mapping nanomechanical properties of live cells using multi-harmonic atomic force microscopy," Nat. Nanotechnol. **6**, 809–814 (2011).
7. K. Jensen, K. Kim, and A. Zettl, "An atomic-resolution nanomechanical mass sensor," Nat. Nanotechnol. **3**, 533–537 (2008).
8. M. S. Hanay, S. Kelber, A. Naik, D. Chi, S. Hentz, E. Bullard, E. Colinet, L. Duraffourg, and M. Roukes, "Single-protein nanomechanical mass spectrometry in real time," Nat. Nanotechnol. **7**, 602–608 (2012).
9. A. N. Cleland and M. L. Roukes, "A nanometre-scale mechanical electrometer," Nature **392**, 160–162 (1998).
10. M. LaHaye, J. Suh, P. Echternach, K. C. Schwab, and M. L. Roukes, "Nanomechanical measurements of a superconducting qubit," Nature **459**, 960–964 (2009).
11. E. Gil-Santos, J. J. Ruz, O. Malvar, I. Favero, A. Lemaître, P. M. Kosaka, S. García-López, M. Calleja, and J. Tamayo, "Optomechanical detection of vibration modes of a single bacterium," Nat. Nanotechnol. **15**, 469–474 (2020).
12. O. Malvar, J. Ruz, P. M. Kosaka, C. M. Domínguez, E. Gil-Santos, M. Calleja, and J. Tamayo, "Mass and stiffness spectrometry of nanoparticles and whole intact bacteria by multimode nanomechanical resonators," Nat. Commun. **7**, 13452 (2016).
13. A. D. O'Connell, M. Hofheinz, M. Ansmann, R. C. Bialczak, M. Lenander, E. Lucero, M. Neeley, D. Sank, H. Wang, M. Weides *et al.*, "Quantum ground state and single-phonon control of a mechanical resonator," Nature **464**, 697–703 (2010).
14. G. Anetsberger, O. Arcizet, Q. P. Unterreithmeier, R. Rivière, A. Schliesser, E. M. Weig, J. P. Kotthaus, and T. J. Kippenberg, "Near-field cavity optomechanics with nanomechanical oscillators," Nat. Phys. **5**, 909–914 (2009).
15. A. B. Ari, M. S. Hanay, M. R. Paul, and K. L. Ekinci, "Nanomechanical measurement of the Brownian force noise in a viscous liquid," Nano Lett. **21**, 375–381 (2020).
16. O. Maillet, X. Zhou, R. Gazizulin, A. M. Cid, M. Defoort, O. Bourgeois, and E. Collin, "Nonlinear frequency transduction of nanomechanical Brownian motion," Phys. Rev. B **96**, 165434 (2017).
17. V. Kara, V. Yakhot, and K. L. Ekinci, "Generalized Knudsen number for unsteady fluid flow," Phys. Rev. Lett. **118**, 074505 (2017).
18. K. Y. Fong, D. Jin, M. Poot, A. Bruch, and H. X. Tang, "Phonon coupling between a nanomechanical resonator and a quantum fluid," Nano Lett. **19**, 3716–3722 (2019).

[19] A. T. Liem, C. Ti, V. Kara, A. B. Ari, J. G. McDaniel, and K. L. Ekinci, "Acoustic radiation of MEMS and NEMS resonators in fluids," J. Appl. Phys. **129**, 064304 (2021).
[20] A. T. Liem, A. B. Ari, C. Ti, M. J. Cops, J. G. McDaniel, and K. L. Ekinci, "Nanoflows induced by MEMS and NEMS: Limits of two-dimensional models," Phys. Rev. Fluids **6**, 024201 (2021).
[21] C. Ti, A. B. Ari, M. C. Karakan, C. Yanik, I. I. Kaya, M. S. Hanay, O. Svitelskiy, M. González, H. Seren, and K. L. Ekinci, "Frequency-dependent piezoresistive effect in top-down fabricated gold nanoresistors," Nano Lett. **21**, 6533 (2021).
[22] T. Low, Y. Jiang, M. Katsnelson, and F. Guinea, "Electron pumping in graphene mechanical resonators," Nano Lett. **12**, 850–854 (2012).
[23] I. Khivrich, A. A. Clerk, and S. Ilani, "Nanomechanical pump–probe measurements of insulating electronic states in a carbon nanotube," Nat. Nanotechnol. **14**, 161–167 (2019).
[24] S. Sapmaz, P. Jarillo-Herrero, Y. M. Blanter, C. Dekker, and H. Van Der Zant, "Tunneling in suspended carbon nanotubes assisted by longitudinal phonons," Phys. Rev. Lett. **96**, 026801 (2006).
[25] T. Kouh, M. S. Hanay, and K. L. Ekinci, "Nanomechanical motion transducers for miniaturized mechanical systems," Micromachines **8**, 108 (2017).
[26] A. N. Cleland and M. L. Roukes, "Noise processes in nanomechanical resonators," J. Appl. Phys. **92**, 2758–2769 (2002).
[27] A. N. Cleland, *Foundations of Nanomechanics: From Solid-State Theory to Device Applications* (Springer Science & Business Media, 2013).
[28] M. Paul, M. Clark, and M. Cross, "The stochastic dynamics of micron and nanoscale elastic cantilevers in fluid: Fluctuations from dissipation," Nanotechnology **17**, 4502 (2006).
[29] M. T. Clark, J. E. Sader, J. P. Cleveland, and M. R. Paul, "Spectral properties of microcantilevers in viscous fluid," Phys. Rev. E **81**, 046306 (2010).
[30] J. E. Sader, "Frequency response of cantilever beams immersed in viscous fluids with applications to the atomic force microscope," J. Appl. Phys. **84**, 64–76 (1998).
[31] I. Bargatin, I. Kozinsky, and M. Roukes, "Efficient electrothermal actuation of multiple modes of high-frequency nanoelectromechanical resonators," Appl. Phys. Lett. **90**, 093116 (2007).
[32] J. W. Wagner, "Optical detection of ultrasound," Phys. Acoust. **19**, 201–266 (1990).
[33] S. Rao, *Vibration of Continuous Systems* (John Wiley & Sons, Inc., 2007).
[34] A. Bokaian, "Natural frequencies of beams under tensile axial loads," J. Sound Vib. **142**, 481–498 (1990).
[35] A. T. Liem, A. B. Ari, J. G. McDaniel, and K. L. Ekinci, "An inverse method to predict NEMS beam properties from natural frequencies," J. Appl. Mech. **87**, 061002 (2020).
[36] C. C. Hopkins and J. R. de Bruyn, "Vibrating wire rheometry," J. Non-Newtonian Fluid Mech. **238**, 205–211 (2016).
[37] P. Malara, R. Zullo, G. Filippone, L. Verdolotti, M. Lavorgna, A. Giorgini, S. Avino, and G. Gagliardi, "Rheology of complex fluids with vibrating fiber-optic sensors," Sens. Actuators, A **264**, 219–223 (2017).
[38] R. T. Erdogan, M. Alkhaled, B. E. Kaynak, H. Alhmoud, H. S. Pisheh, M. Kelleci, I. Karakurt, C. Yanik, Z. B. Sen, B. Sari *et al.*, "Atmospheric pressure mass spectrometry of single viruses and nanoparticles by nanoelectromechanical systems," ACS Nano **16**, 3821 (2022).
[39] S. K. Roy, V. T. Sauer, J. N. Westwood-Bachman, A. Venkatasubramanian, and W. K. Hiebert, "Improving mechanical sensor performance through larger damping," Science **360**, eaar5220 (2018).
[40] M. S. Hanay, S. I. Kelber, C. D. O'Connell, P. Mulvaney, J. E. Sader, and M. L. Roukes, "Inertial imaging with nanomechanical systems," Nat. Nanotechnol. **10**, 339–344 (2015).